Effective Transport Properties for Fuel Cells: Modeling and Experimental Characterization

Chapter 7

Effective transport properties for fuel cells: modeling and experimental characterization

Pablo A. García-Salaberri[1,*] and Prodip K. Das[2]

[1]*Departamento de Ingeniería Térmica y de Fluidos, Universidad Carlos III de Madrid, Madrid, Spain,* [2]*School of Engineering, The University of Edinburgh, Edinburgh, United Kingdom*

Abstract:

Polymer electrolyte fuel cells (PEFCs) are key elements in governments' plans to create a future hydrogen economy, providing clean, affordable electrical power for vehicles and portable electronic devices, among other applications. However, excessive cost and limited performance and durability still limit PEFC commercialization. At this stage of technological development, reducing Pt loading while improving performance and durability requires a tailored design of effective properties (e.g., thermal conductivity and diffusivity) and electrochemical activity (e.g., electrochemical surface area) of porous transport layers. Multifunctional thin, porous layers must be optimized by a combination of modeling and experimental work at different scales, ranging from a single layer up to cell (and stack) level(s). Even though this challenging task has already motivated a large body of work, further research on effective properties through the multiscale pore structure of PEFCs is needed to meet PEFC targets in the coming years.

Key Words: Hydrogen, Fuel Cell, Transportation, Porous Transport Layers, Effective Properties

[*] Corresponding author: pagsalab@ing.uc3m.es

1. Introduction

The demand to reduce the use of hydrocarbons in the automotive sector has intensified in the last decades to mitigate climate change [1,2]. Currently, battery electric vehicles (BEVs) sales exceed 1 million annually, while fuel cell electric vehicles (FCEVs) sales barely exceed 15,000 units around the world (~1%). This sharp difference is explained by the lower level of deployment of hydrogen infrastructure compared to electric vehicle charging stations (about a decade late), together with the current higher capital and operational cost of FCEVs [3]. However, FCEVs present several advantages over BEVs, such as fast refueling times, higher range (~600 km between refueling), larger longevity (above 200,000 km), and better driver experience (similar operation to conventional internal combustion engines with lower anxiety related to lack of range). Thus, the FCEV market is expected to grow gradually in the coming years as production costs on a larger scale are reduced and the availability of hydrogen fueling stations is increased. Similar costs to BEVs may be achieved by 2030. Currently, most major automotive companies have started to commercialize FCEVs, such as Toyota Mirai, Hyundai Nexo, and Honda Clarity, or have included the development of FCEVs in their R&D plans (e.g., Ford Motor Company and Mercedes) [4].

The main barriers hindering widespread commercialization of FCEVs (apart from the scarce development of hydrogen infrastructure) are: (i) high cost associated with the use of Platinum-based catalysts (and other uncommon materials), (ii) insufficient performance and durability, and (iii) lack of economies of scale in FCEV production. In fact, all these aspects are interrelated since high cost and low performance and durability prevent the creation of economies of scale. Changing this situation requires the optimization of components (higher durability and performance at lower cost) used in polymer electrolyte fuel cells (PEFCs). Key aspects to be addressed are the reduction of Pt loading and the development of durable components with improved effective transport properties and electrochemical activity (especially for oxygen reduction at the cathode) [5]. As shown in Figure 7.1, the catalyst represents 40% of the cost of a PEFC system, bipolar plates around 30%, and 20% of the remaining components (membrane, backing layers, and gaskets). The balance of plant (pumps, sensors, compressors, recirculation blowers, etc.) amounts to approximately 10%.

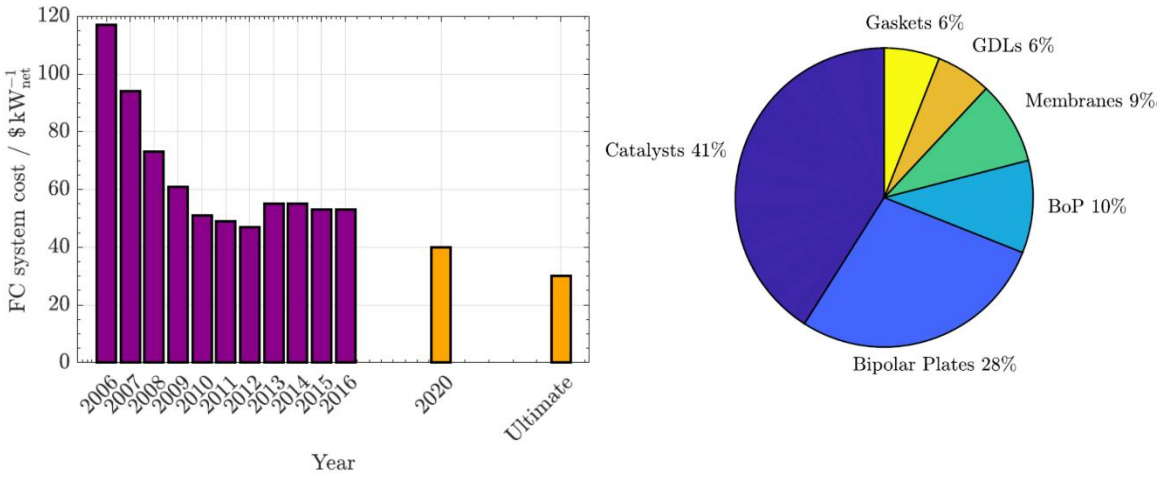

FIGURE 7.1 Evolution of the cost of an 80-kWnet PEM fuel cell system and component cost distribution based on projection to high-volume manufacturing (500,000 units/year).

One of the main issues that complicates the development of high performance, durable components is the small thickness and multifunctional character of thin porous layers in fuel cells. For example, backing layers must fulfill several critical functions, such as providing a transport pathway for reactants and products through its pore volume and ensuring charge and heat conduction through its solid matrix. Recently, Toyota Motor Corporation has shown that fuel cell performance can be significantly improved by the combined optimization of components and operation [6]. For instance, cathode catalysts experience voltage cycles, variable multiphase conditions and repeated start-up/shutdown during operation, which lower performance with time. The design of next-generation PEFCs and porous transport layers therein must be conceived in an integral form, combining electrochemistry, transport in porous media and materials fabrication at different scales.

The aim of this chapter is to analyze the main characteristics and effective transport properties of porous layers present in PEFCs. Modeling and experimental techniques widely used for fuel cell characterization are also discussed. The content is not intended to provide an exhaustive literary review but to provide the reader with an overview of porous transport layers in fuel cells. The chapter is divided into 3 sections. Section 2 is devoted to the structure and composition of porous components. Section 3 is devoted to effective transport properties. And Section 4 is devoted to modeling and experimental techniques. The concluding remarks are presented in Section 5.

2. Structure and composition of porous transport layers in fuel cells

There are several porous transport layers in PEFCs. These include gas diffusion layers (GDLs), microporous layers (MPLs), and catalyst layers (CLs). Every PEFC has one layer of each on both

sides (anode and cathode sides) of the polymer electrolyte (or membrane). Catalyst layers, where the electrochemical reactions take place, are in direct contact with the polymer electrolyte and MPL. Microporous layers are situated in between CLs and GDLs. The purpose of MPLs is to improve water management by providing effective water transport. It also minimizes the contact resistance between the GDL and catalyst layer, limits the loss of catalyst to the GDL interior, and prevents dry-out of the membrane at low current densities or low humidity. GDLs are adjacent to the gas flow channel on both sides of a PEFC and it allows reactant gases to diffuse through to the catalyst layer. Additionally, GDLs provide mechanical support to the cell and allow product water to transport from the catalyst layer to the gas flow channel; thus, preventing water-flooding inside the cathode catalyst layer. Each of these layers has unique composition and structure due to their distinct purposes in a PEFC, as schematically highlighted in Figure 7.2.

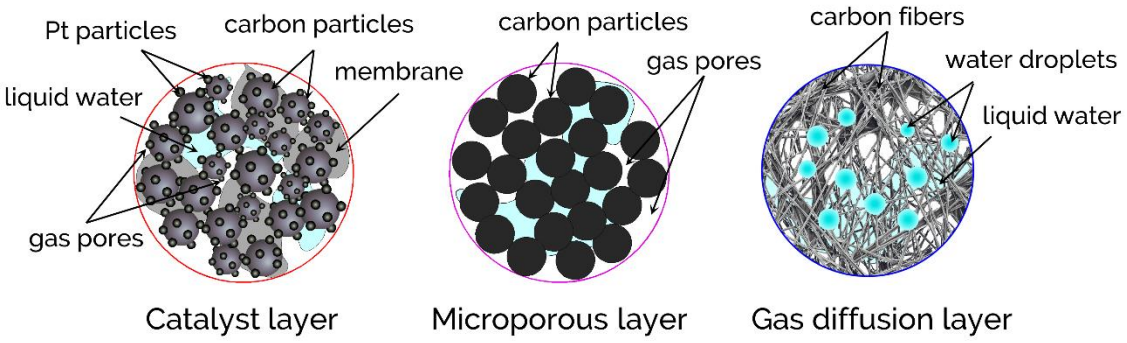

FIGURE 7.2 Schematic illustrations of the structure and composition of catalyst layer, micro-porous layer, and gas diffusion layer for PEFCs [7].

The microstructure of widely used CL for PEFC consists of a matrix of platinum (Pt) catalyst particles supported on carbon particles, electrolyte membrane (also known as ionomer), and void space (pores) with a pathway for electrons and protons to reach the reaction sites. This type of CL is known as the Pt/C CL, as platinum (Pt) nanoparticles are dispersed onto the surfaces of larger carbon black particles. Both the liquid phase and gas phase are co-existing inside the catalyst layers. Thus, the pores can be filled with either liquid water or reactant gases, as shown in Figure 7.2. Alternative to the Pt/C CL is the nanostructured thin film (NSTF) catalyst layer. The key features of the NSTF catalyst layer are low Pt-loading, thinner than Pt/C CL, and it does not have carbon support or any additional ionomer, as the Pt catalyst is directly deposited to form an electronically conductive and electrochemically active layer.

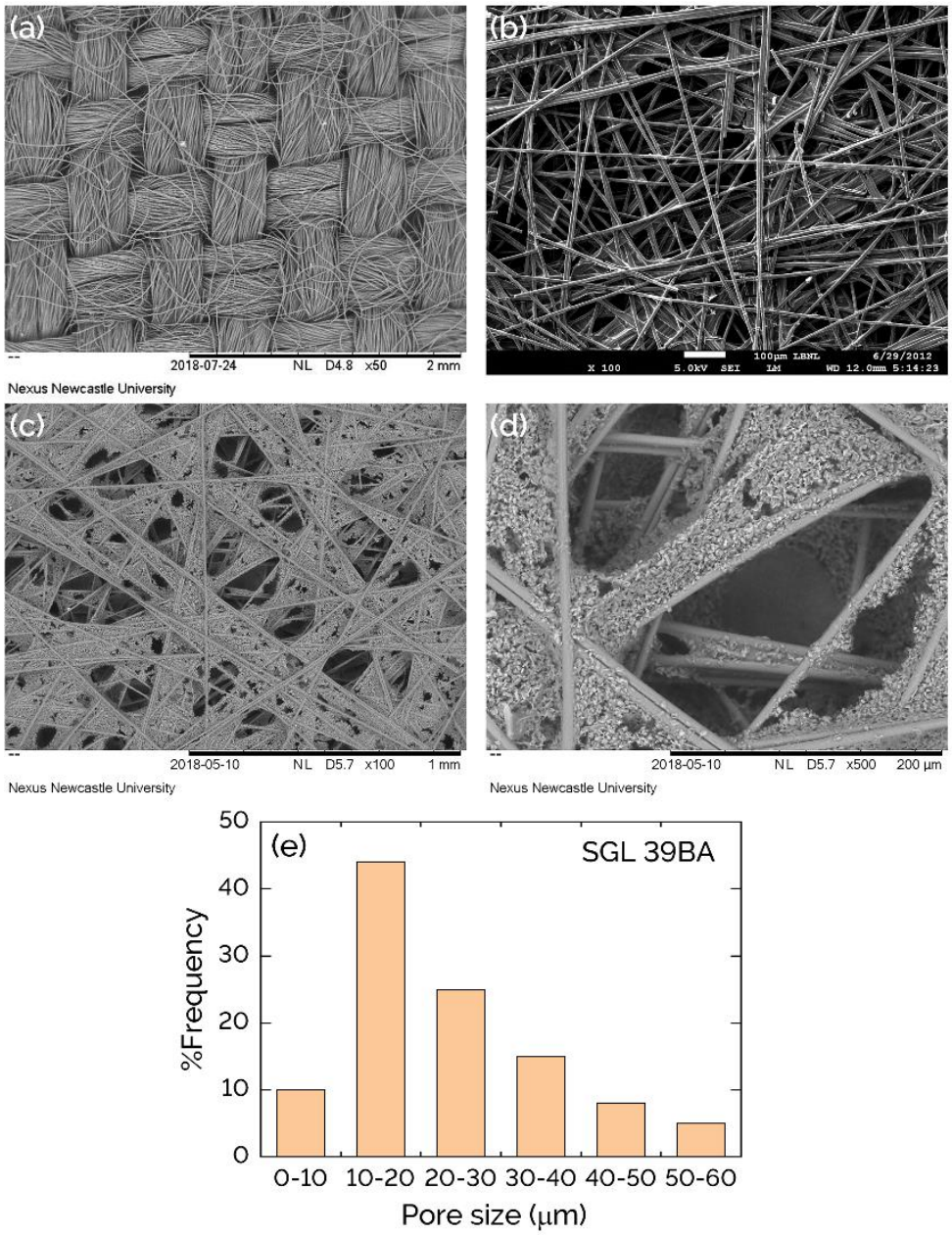

FIGURE 7.3 Scanning electron microscope images of carbon cloth and carbon paper GDLs and pore size distribution of carbon paper GDL. (a) carbon cloth GDL, (b) Toray-TGP-H-120 (0 wt% PTFE loading), (c) SGL 39BA (5 wt% PTFE loading), (d) SGL 39BA (5 wt% PTFE loading), and (e) pore size distribution of SGL 39BA. Pore size distribution data are from Ref. [8]. *Credit: Dr. Deepashree Thumbarathy and Mr. Xiao Liu (Sustainable Energy Systems Lab, Newcastle University, UK), and Weber Lab (Lawrence Berkeley National Laboratory, USA).*

The microporous layer consists of carbon nanoparticles mixed with hydrophobic poly-tetra-fluoro-ethylene (PTFE) and void space with a pathway for electrons to reach the CL. Like CL, MPL pores can also be filled with liquid water and reactant gases during fuel cell operation as well as they provide passage for reactant gases to reach the CL and liquid water to reach the flow channel via

the GDL. The GDLs are made by weaving carbon fibers into a carbon cloth or by pressing carbon fibers together into carbon paper. They are often rendered wet-proof by saturating the pores with PTFE emulsions, followed by drying and sintering to affix the PTFE particles to the carbon fiber to improve liquid transport. The scanning electron microscope images of typical carbon paper GDL and carbon cloth GDL with and without PTFE treatment are shown in Figure 7.3 along with the pore size distributions of SGL 39BA GDL [8]. Comparing Figure 7.3(b) with Figures 7.3(c) and 7.3(d), one can easily distinguish the PTFE loading in the GDL. As the microstructure and composition of CL, MPL, and GDL vary significantly, the key parameter for reactants, water, and electrons transports are porosity, pore size, and wettability also vary significantly. A discussion on these parameters is given below.

Table 7.1: Commonly used Sigracet (SGL) and Toray (TGP) GDLs and their porosity values.

Name	Thickness (μm)	PTFE Treated	MPL	Porosity
SGL 10 BA	400	Yes	No	0.88
SGL 10 BC	420	Yes	Yes	0.80
SGL 24 BA	190	Yes	No	0.84
SGL 24 BC	230	Yes	Yes	0.76
SGL 25 BA	190	Yes	No	0.88
SGL 25 BC	235	Yes	Yes	0.80
SGL 34 BA	280	Yes	No	0.83
SGL 34 BC	315	Yes	Yes	0.75
SGL 39 BA	280	Yes	No	0.80
SGL 39 BC	325	Yes	Yes	0.80
TGP-H-030	110	No	No	0.80
TGP-H-060	190	No	No	0.78
TGP-H-090	280	No	No	0.78
TGP-H-120	370	No	No	0.78

2.1 Porosity and pore size

The porosity of porous transport layers (GDL, CL, and MPL) in fuel cells is the measure of the void spaces. It is represented by the fraction of the volume of voids over the total volume and is often denoted by the symbol, ϕ or ε (varies between 0 and 1). For GDLs that are often made by

weaving carbon fibers into a carbon cloth or by pressing carbon fibers together into a carbon paper, the porosity can be determined by subtracting the volume occupied by the carbon fibers from 1. However, not all pores are connected and there can be PTFE loading in GDL. Thus, experiments (such as mercury porosimetry, Helium pycnometry, or imbibition method) are often used to measure the true porosity of porous transport layers. Typically, the uncompressed porosity of fuel cell GDLs can be between 0.7 and 0.9, while the thickness varies between 100 and 400 μm. Several commonly used GDLs are listed in Table 7.1. The diameter of carbon fibers varies between 5 and 10 μm, while the pore sizes of GDL can vary between 10 and 100 μm. However, most of the pores are between 10 and 40 μm for SGL 39BA GDL as shown in Figure 7.3(e). Microporous layers in fuel cells act as a transition layer between the GDL and CL. Thus, the porosity and pore size of MPLs are always lower than GDLs but higher than CLs. Typical fuel cell MPLs (such as SIGRACET C-type) are often based on carbon nanoparticles mixed with PTFE (roughly 77 wt% carbon black and 23 wt% PTFE). Figure 7.4 shows a scanning electron microscope image of MPL. The typical pore size of such MPL can be between 10 and 200 nm, porosity can be in the 0.3–0.5 range, and the thickness varies between 10 and 50 μm. An SEM image and the pore size distributions of a typical microporous layer are shown in Figure 7.4 [9]. The pore size distribution data presented in Figure 7.4 are taken from Ref. [10].

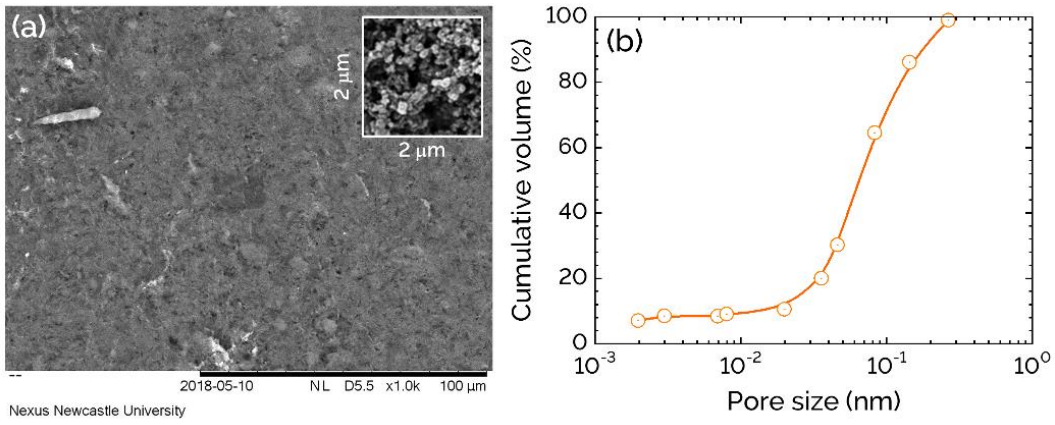

FIGURE 7.4 (a) Scanning electron microscope image of a typical fuel cell MPL and (b) pore size distribution. *Credit: SEM image is reprinted from P.K. Das and D. Thumbarathy, "Chapter 16 - Heat and Fluid Flow in Porous Media for Polymer-Electrolyte Fuel Cells," in Convective Heat Transfer in Porous Media, pp. 341–360, CRC Press, Boca Raton, USA, 2019, with permission from Taylor & Francis.*

Both GDL and MPL have a relatively simpler structure and composition compared with the fuel cell catalyst layer. As the typical Pt/C CL is made of Pt and carbon particles mixed with electrolyte, the pore size and porosity of CL are significantly smaller than that of MPL and GDL due to the

formation of agglomerates of Pt and carbon particles covered with electrolyte. This leads to two types of pores in Pt/C CL: primary pores and secondary pores. Primary pores are between Pt/C particles inside the agglomerates. These pores typically range from 20 to 60 nm. The secondary pores are in between the agglomerates and the void spaces. These pores are usually larger than primary pores and vary between a few hundred nanometers to 50 nm. The porosity of Pt/C CL can be between 0.2 and 0.3, while the thickness of CLs depends on the amount of catalyst loading and varies between 10 and 50 μm. On the other hand, 3M's NSTF catalyst layer is an extended surface catalyst that includes single-crystalline whiskers of an organic compound coated with platinum alloy. NSTF CLs are 20–30 times thinner than conventional Pt/C layers (typically less than 1 μm). Thus, it has significantly lower Pt-loading (in the order of 0.05–0.15 mg-Pt/cm^2). SEM images of conventional Pt/C and 3M's NSTF catalyst layers and the pore size distributions for Pt/C are shown in Figure 7.5 [11, 12]. The pore size distributions for Pt/C are taken from Ref. [13].

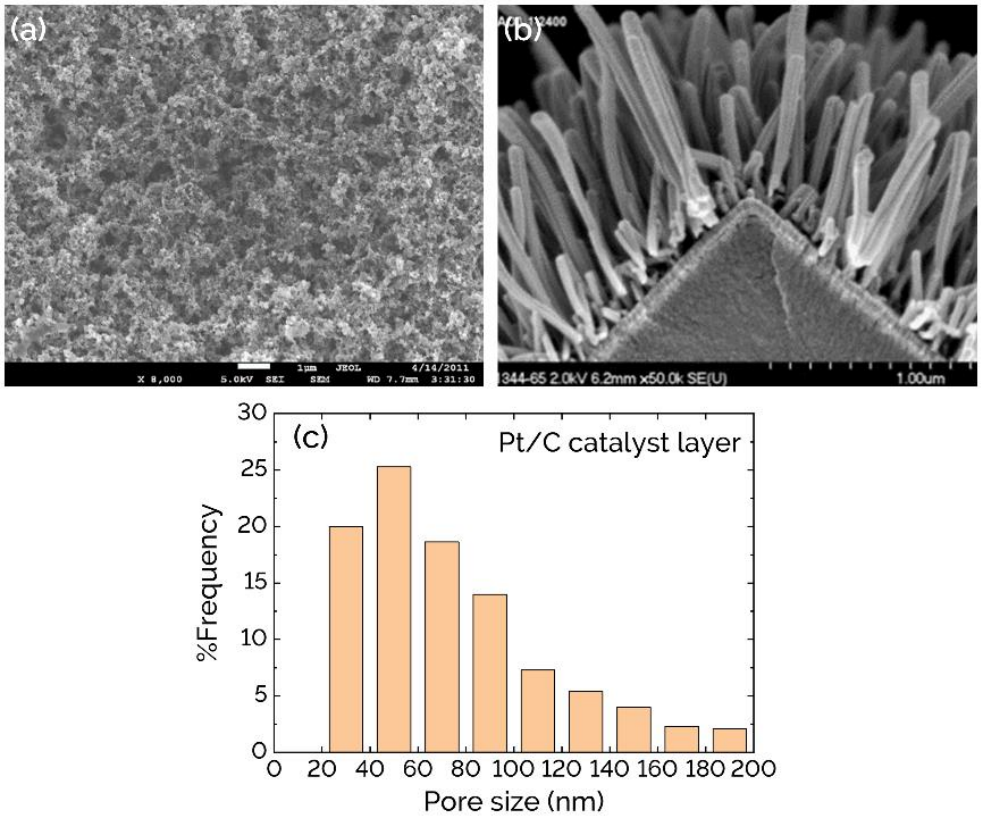

FIGURE 7.5 Scanning electron microscope images of fuel cell catalyst layers and pore size distributions: (a) conventional Pt/C catalyst layer, (b) PtCoMn alloy-based nanostructured thin film (NSTF) catalyst layer, and (c) pore size distribution of conventional Pt/C CL (20 nm increments). *Credit: Adapted with permission from P.K. Das and A.Z. Weber, Proceedings of the ASME 11th Fuel Cell Science, Engineering, and Technology Conference, Paper No. FuelCell2013-18010, 2013 and M.K. Debe, J. Electrochem. Soc., 160(6), F522-F534, 2013.*

2.2 Wettability

As GDLs are available with a wide range of porosity values and thicknesses, they are also available with a wide range of surface wettabilities. The surface wettability is always represented by the static contact angle for smooth surfaces. For GDLs, both static and dynamic contact angles are required for properly analyzing the water-GDL surface interaction due to the inherent surface roughness of GDL surfaces. Conversely, the wettability of GDL pores is often represented through the capillary pressure-saturation relationship rather than using a contact angle measurement. The surface wettability of a GDL is dictated by the amount of PTFE loading on it as well as its surface roughness. Experimental data show that the static contact angle for GDL without PTFE loading (SGL 24AA) can be 141 ± 3 deg [14], while GDL with 5 wt% PTFE loading (SGL 39BA) can be 145 ± 1 deg [8]. It is considered that GDL with 5 wt% PTFE loading would be sufficient for obtaining a pronounced hydrophobicity for typical fuel cell operation. However, a higher PTFE loading may be required for low-temperature fuel cell operation and faster water removal from the GDL surfaces. Experimental data of the static contact angle for GDL with 10, 20, and 30 wt% (SGL 24CA, SGL 24DA, and SGL 24EA) PTFE loadings are reported as 158 ± 2 deg, 159 ± 2 deg, 156 ± 3 deg, respectively [14]. Higher PTFE loadings (>10 wt%) do not provide a higher contact angle as the surface of GDL is statured with PTFE after a certain PTFE loading. At higher PTFE loading, the pore size, however, will be smaller as well as GDL porosity – leading to lower effective transport properties. To overcome the issues with effective transport properties at higher PTFE loading, there are initiatives to selectively modify GDL surfaces with hydrophobic materials instead of the full coverage of PTFE on the GDL surface. For instance, a recent study shows that the GDL surface can be selectively treated using a pattern (such as polka dot, stripes, or checkered) of hydrophobic monomers, such as polydimethylsiloxane (PDMS) matrix containing fumed silica particles or fluorinated ethylene propylene (FEP) [8]. The SEM images of GDLs with selectively modified surface wettability using the stipes PDMS-Si and FEP are shown in Figure 7.6. It has been shown that GDL patterned with FEP can have pore sizes between 5 and 40 μm like the base GDL (SGL 39BA GDL), while GDL patterned with PDMS-Si exhibits slightly smaller pores (5 to 30 μm). However, both FEP-coated and PDMS-Si-coated exhibit significantly higher contact angles, 162° and 159°, respectively compared with a base GDL of 145°. Thus, one can achieve significantly higher surface wettability with the least amount of compromise in GDL pore size and porosity. Moreover, these GDLs can perform better in fuel cells and provide higher limiting currents as compared to base GDLs [8]. This may pave the way to design novel and tunable GDLs for high-power PEFCs.

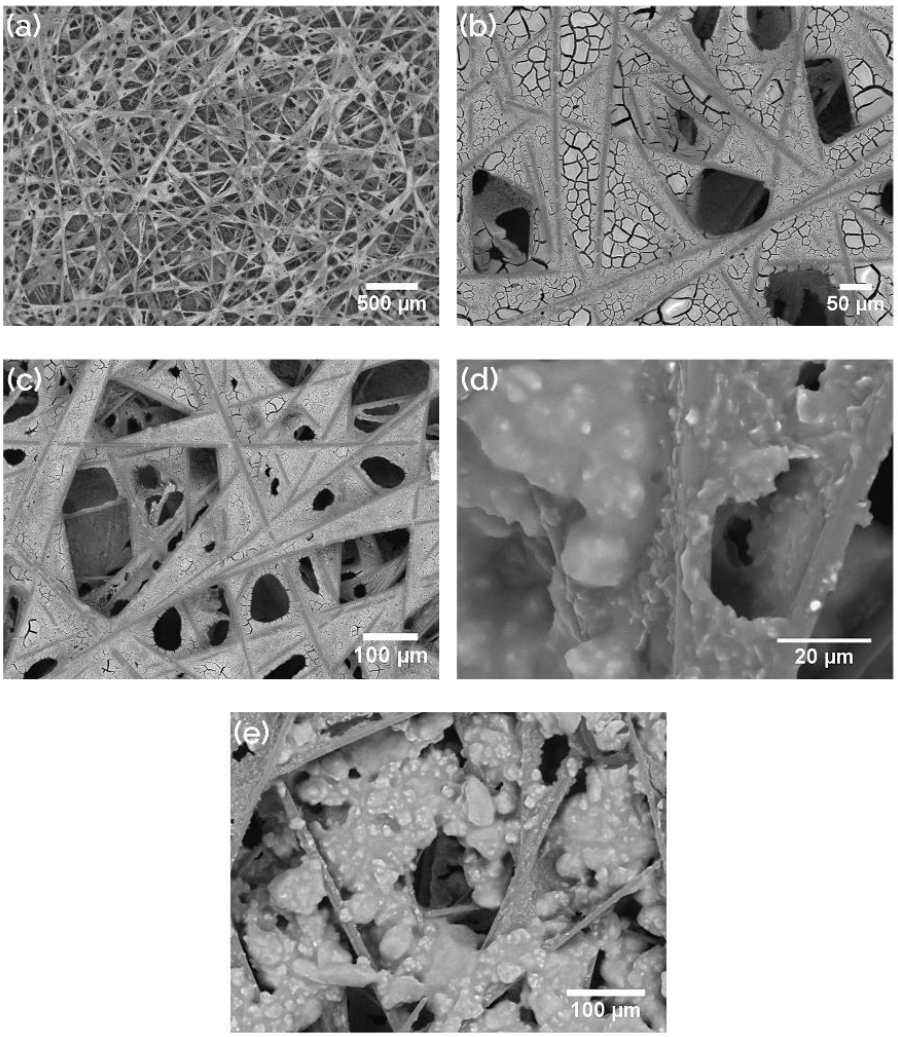

FIGURE 7.6 SEM images of GDLs with selectively modified surface wettability. (a) Base GDL (SGL 39BA), (b) and (c) FEP-coated GDLs, and (d) and (e) PDMS-Si-coated GDLs at various magnifications showing the surface morphology. *Credit: Reprinted from Thumbarathy et al., Journal of Electrochemical Energy Conversion and Storage, 17 (1), 011010-1, 2020, with permission from ASME.*

3. Effective Transport Properties

As discussed above, PEFC's porous transport layers must provide several critical functions, such as providing a transport pathway for reactants and products through the pore volume and ensuring charge and heat conduction through their solid matrix. Catalyst layers have the added functionality of providing an electrochemically active surface area. As shown in Figure 7.7, relevant effective properties include permeability used in Darcy's law, tortuosity factor used to correct Fick's law of diffusion, and effective electrical and thermal conductivities used in Ohm's and Fourier's laws. An

overview of effective diffusivity, local mass transport resistance, permeability, and thermal, electrical, and ionic conductivities of GDLs, MPLs, and CLs is presented below.

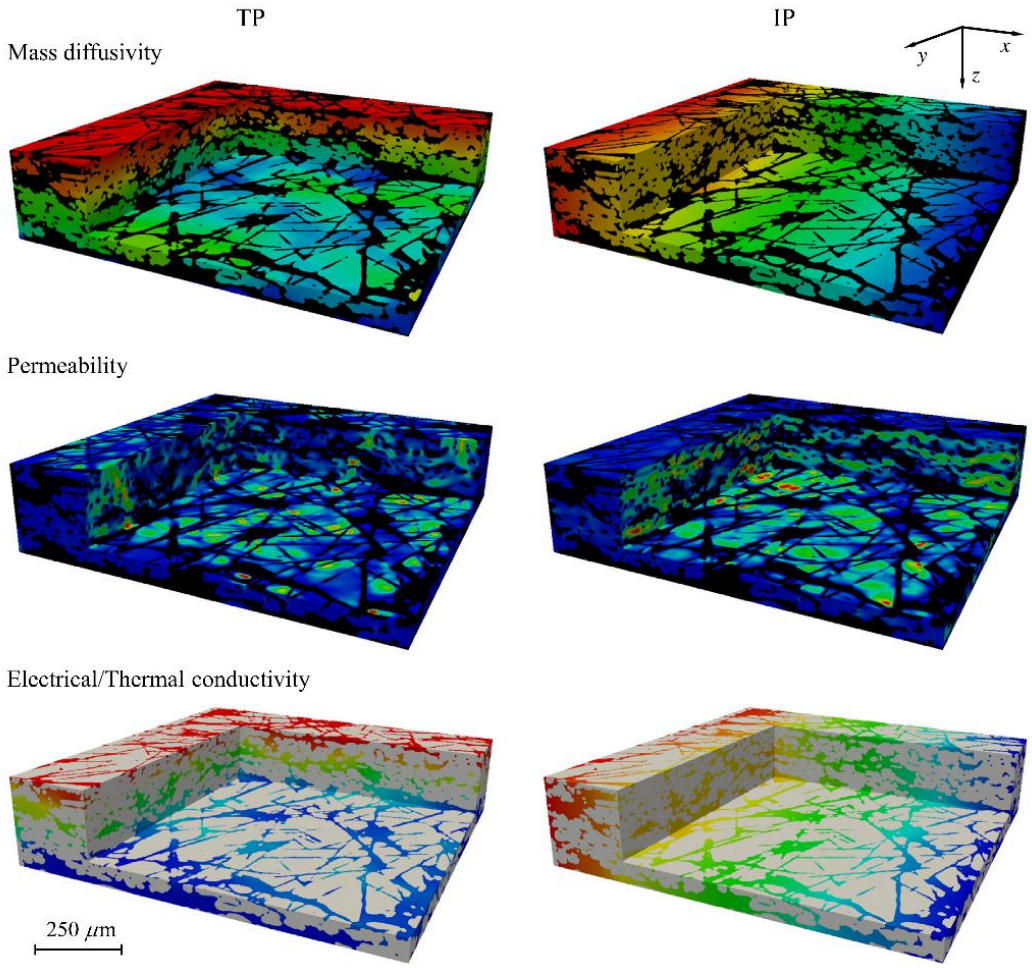

FIGURE 7.7 Concentration, velocity magnitude, and electronic potential/temperature fields, corresponding to calculations of through-plane (TP) and in-plane (IP) effective diffusivity, permeability and effective electrical/thermal conductivity, respectively, on a carbon-paper GDL (10 wt% PTFE-treated TGP-H-120). *Credit: Reprinted from P.A. García-Salaberri et al., International Journal of Heat and Mass Transfer, 127, 687-703, 2018, with permission from Elsevier.*

3.1 Effective diffusivity

Most GDLs, especially carbon paper, show anisotropic effective diffusivity due to the preferential alignment of fibers and pores in the material plane [15]. As shown in Figure 7.8, a higher diffusivity is found in the in-plane direction. The through-plane effective diffusivity is notably lower than predicted by most widely used models, such as Bruggeman's effective medium theory and the random fiber model of Tomadakis and Sotirchos [16,17]. The deviation from these idealized models is caused by the complex structure formed by fibers, binders, and PTFE [18]. Typical

effective diffusivities in the through-plane direction (normalized with respect to the bulk value) are in the range between 0.2-0.4, being 1.5-2 times larger than the effective diffusivity in the material plane.

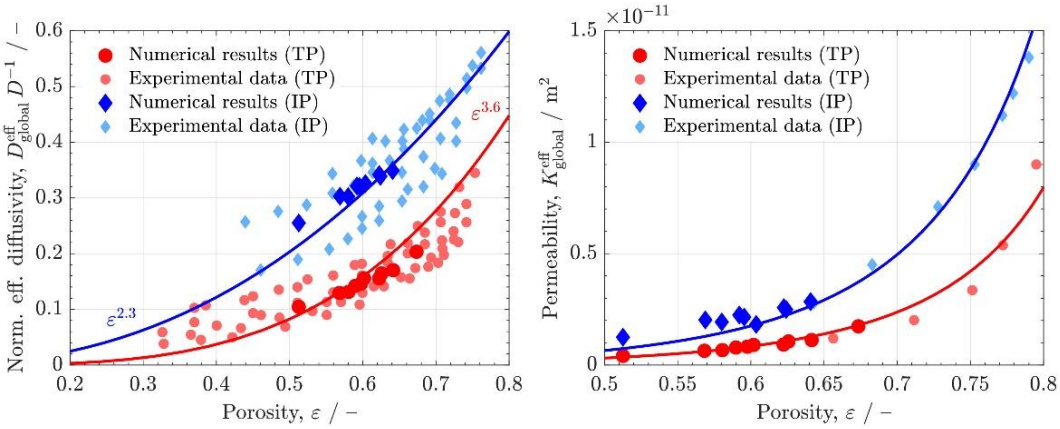

FIGURE 7.8 Normalized effective diffusivity and permeability in the through-plane (TP) and in-plane (IP) directions as a function of GDL compression ratio computed with the hybrid pore network/continuum model presented in [19] compared to previous experimental data. *Credit: Reprinted from P.A. García-Salaberri, International Journal of Heat and Mass Transfer, 167, 120824, 2021, with permission from Elsevier.*

Beyond pore structure, the distribution and amount of liquid water in the pore space (i.e., water saturation) have a strong impact on GDL diffusivity. The relative effective diffusivity, defined as the ratio between the effective diffusivity under wet and dry conditions depends on water saturation as a power law of the form, $g(s)=(1-s)^n$, where the saturation exponent n lies between 2-5 depending on the arrangement of water and peak saturation [20,21] (see Figure 7.9).

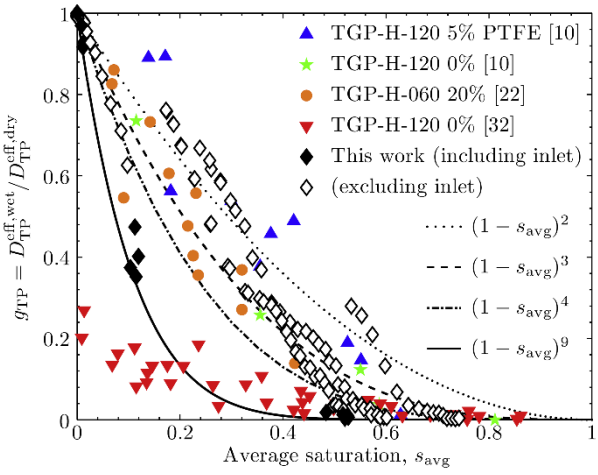

FIGURE 7.9 Through-plane relative effective diffusivity, g_{TP}, as a function of average saturation, s_{avg}, of carbon-paper GDLs (Toray TGP-H-120) determined numerically in Ref. [20] compared to previous experimental data. *Credit: Reprinted from P.A. García-Salaberri et al., International Journal of Heat and Mass Transfer, 86, 319-333, 2015, with permission from Elsevier.*

MPL effective diffusivity has been less examined, usually considering the whole bilayer (GDL+MPL) due to the exceedingly small thickness of MPL coating [22]. The normalized dry effective diffusivity of MPLs is rather isotropic due to the spherical shape of carbon nanoparticles, being around 0.1-0.2 (3-5 times lower than GDLs). The lower diffusivity is explained by the dominant role of Knudsen diffusion in pores smaller than 1 μm due to the frequent collision of molecules with pore walls [23,24]. The effect of water on MPL effective diffusivity is still a source of investigation. A saturation exponent around n=1.5 is assumed in most macroscopic models [25,26].

A growing number of works have been devoted in the last years to CL effective diffusivity due to its critical role in fuel cell performance and durability. CL effective diffusivity is rather isotropic and its normalized value is somewhat lower than that of the MPL (0.1-0.2) because of the Knudsen effect in primary and secondary pores (6-100 nm). CL effective diffusivity can be increased using highly porous open structures, such as those obtained by freeze-drying and electrospraying [27,28]. Achieving high CL diffusivity is important to increase performance when the number of active sites is reduced at low Pt loading [29].

3.2 Local mass transport resistance

In addition to CL diffusivity, the local mass transport resistance from the pore space towards Pt nanoparticles plays a critical role at low cathode Pt loading. As shown in Figure 7.10, the local resistance can be decomposed into five components: (i) the interfacial resistance at the pore/water interface, (ii) the diffusive resistance across the water film, (iii) the interfacial resistance at the water/ionomer interface, (iv) the diffusive resistance across the thin ionomer film, and (v) the interfacial resistance at the ionomer/Pt surface [30]. Recent experimental works have shown that the diffusive resistance across thin ionomer films (1-10 nm in thickness) is dominant, while the interfacial resistances only sum up to one-third of the ionomer resistance [31]. The low oxygen permeability in CL ionomer films is explained by finite-size substrate interactions, which lead to the formation of a dense ionomer region with extremely low diffusivity near the Pt interface. Strategies to mitigate the adverse effect of the local mass transport resistance at low Pt loading include the design of CLs with an increased electrochemically active surface area, high permeation coefficient of oxygen in ionomer, homogeneous ionomer thickness, and nanostructures with super-hydrophobic properties. In addition, low ionic conductivity in exceedingly thin ionomer films must be avoided through a careful design of the multiscale ionomer network.

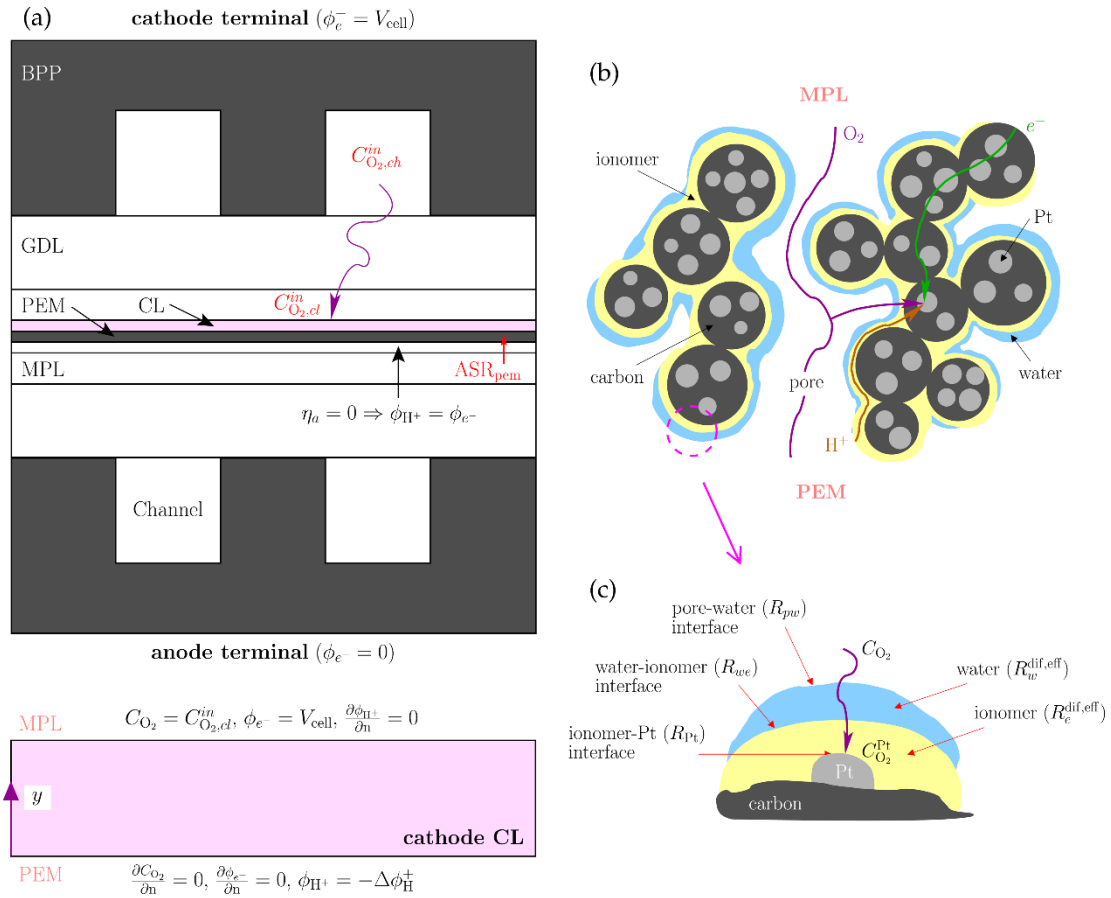

FIGURE 7.10 (a) Schematic of the 1D multiscale model used in [30] to examine oxygen transport resistance in the cathode CL. (b) Sketch of CL microstructure, indicating transport pathways of oxygen, electrons, and protons. (c) Close-up view of oxygen transport resistances from the pore space toward Pt particles. *Credit: Reprinted from A. Sánchez-Ramos et al., Journal of The Electrochemical Society, 168, 124514, 2021 (open access).*

3.3 Permeability

Permeability of fibrous GDLs is also anisotropic, with higher values in the in-plane direction (see Figure 7.8). Permeability of uncompressed GDLs ranges between 10^{-12} and 10^{-11} m^2, decreasing strongly upon compression owing to the decrease of both porosity and pore size [32]. The dependence of GDL permeability on porosity can be well correlated through the Carman-Kozeny equation [33], with a Carman–Kozeny constant in the range $k_{ck} \sim 1 - 100$. Carbon cloth GDLs typically have a higher permeability (lower k_{ck}) and more isotropic character compared to carbon-paper GDLs due to the preferential transport routes provided by large pore sizes between yarns. Permeabilities of MPLs and CLs are significantly lower than that of GDLs, being in the order of $K \sim 10^{-14} - 10^{-13}$ m^2 [34-36]. Lower values prevail in CLs due to the smaller pore sizes of this porous layer.

3.4 Effective thermal conductivity

Effective transport properties that depend on the solid phase usually show a higher degree of anisotropy, reaching values even one order of magnitude larger in the in-plane direction than in the through-plane direction [37]. Such difference is caused by the high interconnectivity of fibers in the material plane unlike infrequent contacts between fibers (and binder) in the through-plane direction. This situation does not hold for effective properties that rely on the fluid phase, which typically show a lower degree of anisotropy. GDL effective thermal conductivity varies significantly between fabrics, from 0.2 to 0.4 $\mathrm{W\,m^{-1}\,K^{-1}}$ (e.g., SGL Carbon's SIGRACET and Mitsubishi Rayon Corporation) up to around 1 $\mathrm{W\,m^{-1}\,K^{-1}}$ (Toray TGP-H series) [38,39]. Key factors affecting the effective thermal conductivity of GDLs include PTFE and binder contents, and assembly compression ratio. The effective thermal conductivity of MPLs and CLs is typically lower than that of GDLs, ranging between 0.1 and 0.15 $\mathrm{W\,m^{-1}\,K^{-1}}$ [40]. The effect of compression on MPL and CL properties is lower due to their smaller pore sizes and stiffness. Further work is still needed to examine the interplay between fuel cell operation and effective thermal conductivity, including interfacial contact resistances, phase change phenomena, and the impact of water saturation on effective thermal conductivity (especially in MPL and CL) [41].

3.5 Effective electrical conductivity

Effective electrical conductivity of GDL, MPL, and CL is high, usually ranging between 10^2 and 10^3 $\mathrm{S\,m^{-1}}$ with a higher anisotropy in GDLs. The fine pore structure of MPL coatings allows a reduction of interfacial contact resistances caused by the macroporous GDL structure [42]. The design of carbon-unsupported CLs, despite their lower use in PEFCs, requires control of ionomer volume fraction and distribution to avoid bottlenecks for electron transport [43].

3.6 Effective ionic conductivity

Effective ionic conductivity of CL and membrane plays a key role in cell performance due to the higher size of protons and thus larger difficulty of proton conduction. For similar volume fractions of the conductive phase (ionomer for proton transport and carbon-Pt for electron transport), membrane effective ionic conductivity (10 $\mathrm{S\,m^{-1}}$) is around two orders of magnitude lower than the electrical conductivity of porous layers ($10^2 - 10^3$ $\mathrm{S\,m^{-1}}$) [30]. Moreover, CL effective ionic conductivity is ten-fold lower than that of the bulk membrane, being in the range 0.05-5 $\mathrm{S\,m^{-1}}$ under well-humidified conditions. CL effective ionic conductivity increases with ionomer volume fraction but remains constant for exceedingly high ionomer volume fractions. This is explained by the increase of the tortuosity factor of the ionomer network at high ionomer volume fractions [44].

The tailored design of the multiscale CL ionomer structure is crucial to optimizing the coupling between proton conduction, oxygen diffusion, and water transport in low Pt-loading CLs.

4. Modeling and experimental techniques

A close combination of experimental and modeling work is essential to examine multiphysics phenomena and guide the design of novel components and cell architectures. The variety of transport phenomena that take place in PEFCs at different scales makes it necessary the use of models with different levels of sophistication according to their dimensionality and resolution of porous media microstructure. Moreover, experimental work involves different disciplines, such as the characterization of single and two-phase effective transport properties, ohmic resistances, and electrochemical performance. An overview of modeling and experimental techniques used in PEFCs (and related electrochemical devices) is presented below.

4.1 Modeling

As shown in Figure 7.11, three main modeling techniques are used to examine mass, charge, and heat transport in porous transport layers: (i) macroscopic modeling, (ii) pore-scale modeling, and (iii) hybrid modeling (i.e., a combination of both macroscopic continuum and pore-scale formulations).

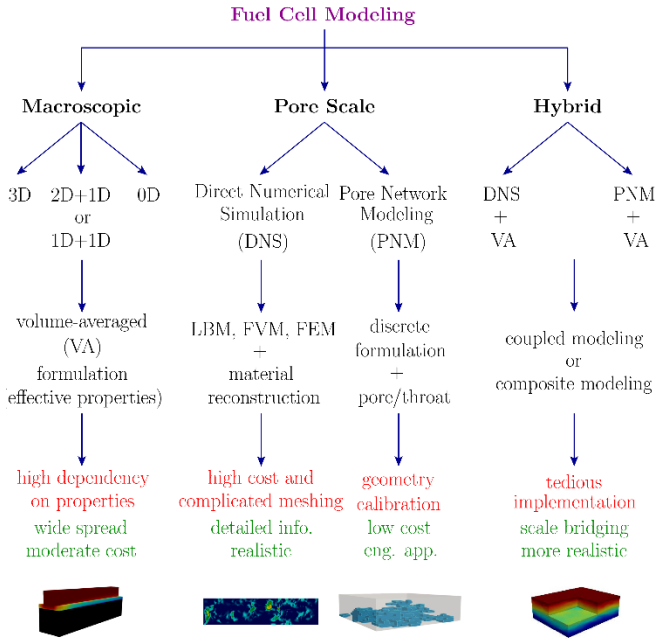

FIGURE 7.10 Flow chart of the three main modeling approaches used to examine transport in PEFCs according to their microstructural resolution. *Credit: Reprinted from P.A. García-Salaberri, General aspects in the modeling of fuel cells: from conventional fuel cells to nano fuel cells, Nanotechnology in Fuel Cells, Micro and Nano Technologies, pp. 77-121, 2022.*

Macroscopic modeling relies on a volume average description of conservation equations in porous components, including mass, momentum, energy, species (H_2, O_2, N_2, and H_2O), electronic and protonic charge, membrane water content, and liquid water. The formulation is closed through constitutive relationships that define effective transport properties of porous components as a function of macroscopic properties (e.g., porosity, water saturation, ionomer volume fraction, etc.). Macroscopic continuum modeling is the most extended approach to analyzing transport at the cell/stack scale due to moderate computational cost and availability of multiphysics models in (commercial) CFD codes [26,45].

Two modeling approaches are used at the pore scale: pore network modeling (PNM) and direct numerical simulation (DNS). PNM idealizes the pore space of porous layers as a network of pore bodies interconnected by throats. The size, shape, and coordination number of the pore/throat assembly are determined according to porous media microstructure. Multiple transport processes can be simulated in the network, such as capillarity, diffusion, convection, etc. [46]. The development of dual networks incorporating both fluid and solid phases has also become increasingly common to analyze, e.g., two-phase transport in GDLs [47]. On the other hand, DNS solves conservation equations directly on microstructures taken from segmented tomography images or virtual reproductions generated by mathematical algorithms [48]. The latter method is generally used to overcome limitations of tomography images, such as the impossibility to differentiating binder and PTFE in GDLs, and ionomer and Pt nanoparticles in CLs. Comparatively, PNM offers a significantly lower computational cost than DNS, although the accuracy of results largely depends on pore network calibration. Hence, PNM is better suited to perform parametric analysis at the microstructural level in engineering applications, while DNS is recommended for the extraction of detailed information during porous material design. Both modeling techniques can also be used to determine effective transport properties for macroscopic models [37].

The use of hybrid models, which combine macroscopic continuum and pore-scale modeling techniques, has recently increased. The aim of hybrid models is to combine in a single framework the strengths of both modeling techniques, i.e., the ease of implementation of continuum approaches in CFD codes and explicit microstructural information from the pore-scale [19]. This type of modeling is particularly useful to improve the predictions of two-phase transport through the multiscale pore structure of MEAs, while accounting for variations of operating conditions and heterogeneities at the cell scale [49]. The combination of PNM and continuum modeling is

preferred in engineering applications due to its lower computational time. In particular, the computational cost arising from the coupling of DNS and continuum modeling can be prohibitive under two-phase conditions due to the wide range of spatial and temporal scales involved in the problem [42].

In addition to the previous three modeling approaches, a large body of work is also devoted to analytical and semi-analytical modeling of effective properties (see Refs. [50,51]). Prediction of effective transport properties based on a simplified representation of the geometry of representative elementary volumes is useful for the fundamental understanding of transport processes and examination of multi-component materials. Moreover, analytical and semi-analytical models can be incorporated into macroscopic, pore-scale, and hybrid models when all spatial and temporal scales cannot be resolved due to excessive computational cost [30]. This practice is common, for example, for the catalyst layer, where transport in agglomerates or around carbon nanoparticles is described by an analytical or semi-analytical sub-model. The large-scale model and the nano-scale sub-model can be coupled by continuity of fluxes or any other physical condition [52].

4.2 Experimental

A wide variety of in-situ characterization, diagnostic, and visualization techniques are available to examine fuel cell operation depending on the physics and materials, and spatial and temporal scales involved. Techniques include traditional methods, such as electrochemical impedance spectroscopy (EIS) or limiting current method, and more novel technologies, such as in-operando X-ray computed tomography and neutron imaging (e.g., for visualization of water transport in GDLs) and segmented cells to track the evolution of local current density, temperature, and membrane resistance [53-57]. These in-situ techniques are complemented with information from the ex-situ characterization of multifunctional components (see, e.g., [58,59]). Figure 7.12 shows a flow chart of widely used methods for the characterization of porous transport layers (GDL, MPL, and CL) effective properties, including (i) structural and morphological properties, (ii) effective transport properties, (iii) mechanical properties, and (iv) electrochemical properties. For completeness, techniques used to characterize some relevant properties of polymeric materials (i.e., membrane) are also considered.

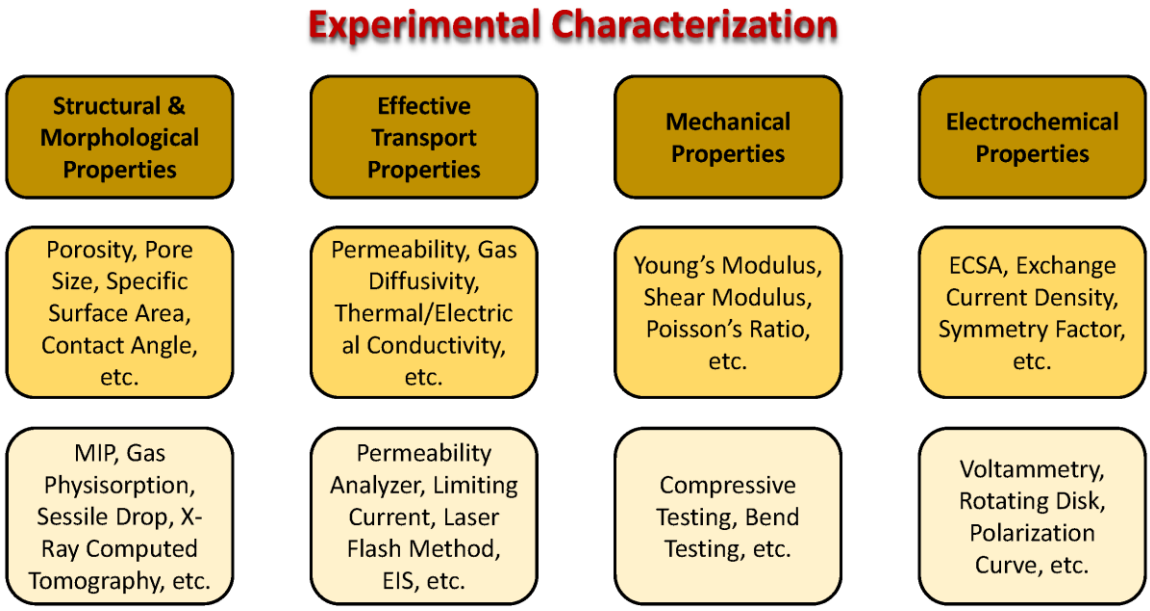

FIGURE 7.12 Flow chart of experimental techniques used for characterization of structural and morphological properties, effective transport properties, mechanical properties, and electrochemical properties in PEFCs.

Common structural and morphological properties of porous transport layers characterized experimentally include porosity, PTFE content, specific surface area, and wettability, among others. Porosity can be measured using Archimedes' principle by weighing porous samples both dry and submerged in a wetting fluid and subsequently determining the solid volume. This technique has been successfully applied to thin porous media (GDL-MPLs and CLs) with high precision in previous works [60,61]. Pore size distribution (PSD) is usually characterized by mercury intrusion porosimetry (MIP) [62]. Modern equipment allows invasion pressures up to 60,000 bar with a resolution down to 3.6 nm. However, nanometric PSDs can also be measured by gas physisorption (using the same equipment to determine Brunauer-Emmett-Teller (BET) surface area), thus avoiding sample alterations caused by exceedingly high pressures [63]. Alternatively, porosity and PSD can also be determined from tomography images. Porosity is simply calculated by voxel counting, while PSD is calculated by determining the size of the largest inscribed sphere containing a certain voxel [20,21]. Unlike MIP experiments, working with tomography images removes any influence caused by the invasion history of mercury from the exterior of a sample. Wettability is frequently characterized through contact angle measured by the sessile drop method [14, 64]. In this technique, a water droplet is placed on the surface of a sample and the contact angle is measured by fitting a tangent to the three-phase point where the liquid surface touches the porous surface. The visualization of material microstructure is usually carried out with a scanning electron microscope (SEM). Quantification of internal contact angles in porous layers is more complicated

but can be accomplished by analysis of tomography images taken during water invasion experiments [65]. Other common techniques used to examine the composition of porous layers are thermogravimetric analysis (e.g., PTFE volume fraction in GDL), elemental analysis with energy-dispersive X-ray spectroscopy, EDX, and X-ray photoelectron spectroscopy, XPS (e.g., the composition of ionomer, carbon, and Pt in CL) and positron annihilation lifetime spectroscopy, PALS (e.g., free volume fraction in ionomer) [60,66,67].

Permeability can be measured with a permeability tester according to Darcy's law. In this apparatus, gas is fed through a sample at a prescribed flow rate (measured with a flow meter) and the resultant pressure drop is recorded (measured with a differential pressure sensor) [33]. Permeability in different directions can be determined by changing the transport direction in the experiments. Different methods have been used to measure the effective diffusivity of thin GDL-MPLs and CLs, including a diffusion bridge, Loschmidt cell, and electrochemical limiting-current method, as well as transient methods in which concentration evolution is fitted against an analytical solution of Ficks' law [68,69]. Effective thermal conductivity has been mostly characterized using in-house setups by measuring the temperature gradient across samples subjected to a heat flux. The contribution of other thermal resistances in the setup (e.g., interfacial resistances) is subtracted to isolate the porous sample resistance and determine effective thermal conductivity [70]. Another technique employed for the characterization of effective thermal conductivity is the laser flash method. This technique is based on the detection of the transient temperature rise on the backside of a sample when it is heated with an energy pulse [71]. Effective electrical conductivity of porous layers is commonly measured by the four-point probe method using separate pairs for current-carrying and voltage-sensing electrodes. The setup with four probes introduces almost negligible contact and spreading resistances associated with voltage probes, thereby providing high accuracy [72]. Effective ionic conductivity is characterized by either direct current (DC) or alternating current (AC) methods using a four-point probe setup and EIS, respectively [44,73]. Similar results have been historically obtained with both methods, even though EIS is more extended due to the widespread availability of electrochemical cells. Moreover, EIS facilitates conductivity measurements in ultra-thin layers, such as CLs. The main drawback of EIS is the need to select an appropriate equivalent circuit for the correct interpretation of AC Nyquist plots.

Analysis of two-phase transport in PEFCs requires the characterization of several additional transport properties, such as water retention curves in porous layers, breakthrough pressure, and droplet adhesion forces at the GDL/channel interface [14, 75.]. Quasi-static transport of water (or

other invading fluids) during drainage and imbibition can be characterized by the method of standard porosimetry (MSP) or volume displacement method [74]. The purpose of these experiments is to measure the amount of water in a sample at fixed capillary pressure. Special care must be taken with evaporation in thin porous media due to the small water volumes used in the experiments. Droplet adhesion force can be measured, e.g., by using a rotating-stage goniometer while injecting water from the bottom or by placing droplets with a syringe on the sample surface [14, 75].

Other relevant effective transport properties in fuel cells are electroosmotic drag coefficient and diffusivity of water in the membrane, permeability of gas species across the membrane, water sorption isotherm of membrane and CL, and electrical and thermal contact resistances. For brevity, the reader is referred to focused reviews [53,54,76].

Mechanical properties of porous layers include anisotropic Young's modulus, shear modulus, and Poisson's ratio. Young's modulus in the through-plane direction is typically measured in compressive tests with universal test machines adapted to thin porous layers, such as those used for packaging applications [77]. Hysteretic behavior at compression can be evaluated in loading-unloading cyclic tests. Young's modulus in the material plane can be determined using different loading conditions, such as tension, compression, or bending. Conditions in fuel cells (a mixture of tension and compression) are better reproduced with 2-point, 3-point, or 4-point bending tests. Measurement of shear modulus and Poisson's ratio is carried out in ad-hoc apparatuses due to the difficulty to determine these properties in thin porous layers. Viscoelastic properties of polymeric materials are also measured in cyclic and relaxation experiments as a function of temperature and relative humidity [78].

Among electrochemical properties, electrochemical surface area (ECSA) and exchange current density are key parameters to evaluate CL performance. ECSA of Pt-based electrocatalysts is calculated in electrochemical cells from the hydrogen adsorption/desorption region of cyclic voltammetry curves after correcting for double-layer charging current. The rotating disk electrode is a useful technique for determining exchange current density and symmetry factors of electrochemical kinetics [79]. However, experiments in hydrogen pump cells and PEFCs are also a common practice to determine electrochemical parameters in conditions closer to the final application [80,81]. The voltage drop in the electrochemical cell is broken down into activation and ohmic losses to isolate the contribution of the former (mass transport losses can be neglected).

Electrochemical parameters are then determined by fitting results to a kinetics expression, usually Tafel or Butler-Volmer kinetics. Additional electrochemical techniques widely employed to obtain electrocatalytic information are linear sweep voltammetry and CO-stripping voltammetry [53].

5. Final remarks

Polymer electrolyte fuel cells (PEFCs) are promising candidates as clean power sources for the transportation sector (e.g., submarines, trains, and light-duty and heavy-duty vehicles). However, their market penetration is still hindered by excessive cost and insufficient performance and durability, thus preventing economies of scale. In the last decades, leading automotive companies have devoted large investments in research and development to optimize and commercialize PEFC technology. However, the progress achieved is not yet sufficient to compete with traditional (e.g., internal combustion engine) and alternative (e.g., battery electric vehicle) technologies. Apart from the need for hydrogen infrastructure, one of the major issues of PEFCs is the large amount of Pt needed to maintain acceptable performance and durability. To overcome this situation and reduce Pt loading, while increasing performance and durability, optimal design of multifunctional porous layers with improved effective properties and electrochemical activity is crucial. This task is complicated by the wide variety of multiphysics, multiphase, and multiscale transport processes that take place in PEFC porous layers. Future PEFC designs must focus not only on the optimization of the cathode catalyst layer microstructure but the integral optimization of the full membrane electrode assembly and flow field (e.g., using 3D printing).

References

1. G. Claeys et al., How to make the European Green Deal work, Policy Contribution 13 (2019) 1-21, https://www.jstor.org/stable/resrep28626
2. M.M. Whiston et al., Expert elicitation on paths to advance fuel cell electric vehicles, Energy Policy 160 (2022) 112671, https://doi.org/10.1016/j.enpol.2021.112671
3. M.M. Whiston et al., Expert assessments of the cost and expected future performance of proton exchange membrane fuel cells for vehicles, Proc. Natl. Acad. Sci. 116 (2019) 4899-4904, https://doi.org/10.1073/pnas.1804221116
4. C.E. Thomas, Fuel cell and battery electric vehicles compared, Int. J. Hydrog. Energy 34 (2009) 6005-6020, https://doi.org/10.1016/j.ijhydene.2009.06.003
5. A. Kongkanand, M.F. Mathias, The priority and challenge of high-power performance of low-platinum proton-exchange membrane fuel cells, J. Phys. Chem. Lett. 7 (2016) 1127-1137, 10.1021/acs.jpclett.6b00216
6. T. Yoshida, K. Kojima, Toyota MIRAI fuel cell vehicle and progress toward a future hydrogen society, Electrochem. Soc. Interface 24 (2015) 45, https://doi.org/10.1149/2.F03152if
7. P.K. Das, Transport Phenomena in Cathode Catalyst Layer of PEM Fuel Cells, University of Waterloo, Waterloo, 2010, http://hdl.handle.net/10012/5282

8. D. Thumbarathy et al., Fabrication and Characterization of Tuneable Flow-Channel/Gas-Diffusion-Layer Interface for Polymer Electrolyte Fuel Cells, J. Electrochem. Energy Convers. Storage 17 (2020) 011010, https://doi.org/10.1115/1.4044814
9. P.K. Das, D. Thumbarathy, Heat and Fluid Flow in Porous Media for Polymer-Electrolyte Fuel Cells, in: Y. Mahmoudi, K. Hooman, K. Vafai (Eds.), Convective Heat Transfer in Porous Media, CRC Press, 2019.
10. J. Becker et al., A multi-scale approach to material modeling of fuel cell diffusion media, Int. J. Heat Mass Transf. 54 (2011) 1360-1368, https://doi.org/10.1016/j.ijheatmasstransfer.2010.12.003
11. P.K. Das, A.Z. Weber, Water Management in PEMFC with Ultra-Thin Catalyst-Layers, Proc. ASME 11th Fuel Cell Science, Engineering, and Technology Conference, FuelCell2013-18010, V001T01A002, 2013.
12. M.K. Debe, Tutorial on the Fundamental Characteristics and Practical Properties of Nanostructured Thin Film (NSTF) Catalysts, J. Electrochem. Soc. 160 (2013) F522-F534, https://doi.org/10.1149/2.049306jes
13. H. Schulenburg et al., 3D Imaging of Catalyst Support Corrosion in Polymer Electrolyte Fuel Cells, J. Phys. Chem. C 115 (2011) 14236-14243, https://doi.org/10.1021/jp203016u
14. P.K. Das et al., Liquid-Water-Droplet Adhesion-Force Measurements on Fresh and Aged Fuel-Cell Gas-Diffusion Layers, J. Electrochem. Soc. 159 (2012) B489-B496, https://doi.org/10.1149/2.052205jes
15. M.F. Mathias, J. Roth, J. Fleming, W. Lehnert, Diffusion media materials and characterization, Handb. Fuel Cells 3 (2010) 517–537.
16. M.M. Tomadakis, S.V. Sotirchos, Ordinary, transition, and Knudsen regime diffusion in random capillary structures, Chem. Eng. Sci. 48 (1993) 3323-3333.
17. B. Tjaden et al., On the origin and application of the Bruggeman correlation for analysing transport phenomena in electrochemical systems, Curr. Opin. Electrochem. 12 (2016) 44–51, https://doi.org/10.1016/j.coche.2016.02.006
18. R. Flückiger et al., Anisotropic, effective diffusivity of porous gas diffusion layer materials for PEFC, Electrochim. Acta 54 (2008) 551–559, https://doi.org/10.1016/j.electacta.2008.07.034
19. P.A. García-Salaberri, Modeling diffusion and convection in thin porous transport layers using a composite continuum-network model: Application to gas diffusion layers in polymer electrolyte fuel cells, Int. J. Heat Mass Transf. 167 (2021) 120824, https://doi.org/10.1016/j.ijheatmasstransfer.2020.120824
20. P.A. García-Salaberri et al., Effective diffusivity in partially-saturated carbon-fiber gas diffusion layers: Effect of through-plane saturation distribution, Int. J. Heat Mass Transf. 86 (2015) 319–333, https://doi.org/10.1016/j.ijheatmasstransfer.2015.02.073
21. P.A. García-Salaberri et al., Effective diffusivity in partially-saturated carbon-fiber gas diffusion layers: Effect of local saturation and application to macroscopic continuum models, J. Power Sources 296 (2015) 440–453, https://doi.org/10.1016/j.jpowsour.2015.07.034
22. M.S. Ismail et al., Effective diffusivity of polymer electrolyte fuel cell gas diffusion layers: An overview and numerical study, Int. J. Hydrog. Energy 40 (2015) 10994–11010, https://doi.org/10.1016/j.ijhydene.2015.06.073
23. C. Chan et al., Experimental measurement of effective diffusion coefficient of gas diffusion layer/microporous layer in PEM fuel cells, Electrochim. Acta 65 (2012) 13–21, https://doi.org/10.1016/j.electacta.2011.12.110
24. M. Göbel et al., Multi-scale structural analysis of gas diffusion layers, J. Power Sources 355 (2017) 8–17, https://doi.org/10.1016/j.jpowsour.2017.03.086
25. P.A. García-Salaberri et al., Hydration and dehydration cycles in polymer electrolyte fuel cells operated with wet anode and dry cathode feed: A neutron imaging and modeling

study, J. Power Sources 359 (2017) 634–655, https://doi.org/10.1016/j.jpowsour.2017.03.155
26. A.Z. Weber et al., A Critical Review of Modeling Transport Phenomena in Polymer-Electrolyte Fuel Cells, J. Electrochem. Soc. 161 (2014) F1254, https://doi.org/10.1149/2.0751412jes
27. K. Talukdar et al., Minimizing mass-transport loss in proton exchange membrane fuel cell by freeze-drying of cathode catalyst layers, J. Power Sources 427 (2019) 309-317, https://doi.org/10.1016/j.jpowsour.2019.04.094
28. Y. Kim et al., Fabrication of platinum group metal-free catalyst layer with enhanced mass transport characteristics via an electrospraying technique, Mater. Today Energy 20 (2021) 10064, https://doi.org/10.1016/j.mtener.2021.100641
29. A.Z. Weber, A. Kusoglu, Unexplained transport resistances for low-loaded fuel-cell catalyst layers, J. Mater. Chem. A 41 (2014) 7207-17211, https://doi.org/10.1039/C4TA02952F
30. A. Sánchez-Ramos et al., Modeling the Effect of Low Pt loading Cathode Catalyst Layer in Polymer Electrolyte Fuel Cells: Part I. Model Formulation and Validation, J. Electrochem. Soc. 168 (2021) 124514, https://doi.org/10.1149/1945-7111/ac4456
31. T. Schuler et al., Fuel-Cell Catalyst-Layer Resistance via Hydrogen Limiting-Current Measurements, J. Electrochem. Soc. 166 (2019) F3020, https://doi.org/10.1149/2.0031907jes
32. L. Holzer et al., Microstructure-property relationships in a gas diffusion layer (GDL) for Polymer Electrolyte Fuel Cells, Part I: effect of compression and anisotropy of dry GDL, Electrochim. Acta 227 (2017) 419-434, https://doi.org/10.1016/j.electacta.2017.01.030
33. J.T. Gostick et al., In-plane and through-plane gas permeability of carbon fiber electrode backing layers, J. Power Sources 162 (2006) 228-238, https://doi.org/10.1016/j.jpowsour.2006.06.096
34. M.S. Ismail et al., Effect of polytetrafluoroethylene-treatment and microporous layer-coating on the in-plane permeability of gas diffusion layers used in proton exchange membrane fuel cells, J. Power Sources 195 (2010) 6619–6628, https://doi.org/10.1016/j.jpowsour.2010.04.036
35. O.M. Orogbemi, et al., The effects of the composition of microporous layers on the permeability of gas diffusion layers used in polymer electrolyte fuel cells, Int. J. Hydrog. Energy 41 (2016) 21345–21351, https://doi.org/10.1016/j.ijhydene.2016.09.160
36. J. Zhao et al., Gas permeability of catalyzed electrodes in polymer electrolyte membrane fuel cells, Appl. Energy 209 (2018) 203–210, https://doi.org/10.1016/j.apenergy.2017.10.087
37. P.A. García-Salaberri et al., Analysis of representative elementary volume and through-plane regional characteristics of carbon-fiber papers: diffusivity, permeability and electrical/thermal conductivity, Int. J. Heat Mass Transf. 127 (2018) 687-703, https://doi.org/10.1016/j.ijheatmasstransfer.2018.07.030
38. H. Sadeghifar et al., Effect of Polytetrafluoroethylene (PTFE) and micro porous layer (MPL) on thermal conductivity of fuel cell gas diffusion layers: Modeling and experiments, J. Power Sources 248 (2014) 632-641, https://doi.org/10.1016/j.jpowsour.2013.09.136
39. N. Zamel, Measurement of the through-plane thermal conductivity of carbon paper diffusion media for the temperature range from− 50 to+ 120° C, Int. J. Hydrog. Energy 36 (2011) 12618-12625, https://doi.org/10.1016/j.ijhydene.2011.06.097
40. Zhang, J. et al., A review of the microporous layer in proton exchange membrane fuel cells: Materials and structural designs based on water transport mechanism, Renew. Sust. Energ. Rev. 156 (2022) 111998, https://doi.org/10.1016/j.rser.2021.111998

41. A.D. Shum et al., Investigating phase-change-induced flow in gas diffusion layers in fuel cells with X-ray computed tomography, Electrochim. Acta 256 (2017) 279-290, https://doi.org/10.1016/j.electacta.2017.10.012
42. P.A. García-Salaberri et al., Implications of inherent inhomogeneities in thin carbon fiber-based gas diffusion layers: A comparative modeling study, Electrochim. Acta 295 (2019) 861-874, https://doi.org/10.1016/j.electacta.2018.09.089
43. P.A. García-Salaberri, 1D two-phase, non-isothermal modeling of a proton exchange membrane water electrolyzer: An optimization perspective, J. Power Sources 521 (2022) 230915, https://doi.org/10.1016/j.jpowsour.2021.230915
44. D.C. Sabarirajan et al., Determining proton transport in pseudo catalyst layers using hydrogen pump DC and AC techniques, J. Electrochem. Soc. 167 (2020) 084521, https://doi.org/10.1149/1945-7111/ab927d
45. P.A. García-Salaberri, General aspects in the modeling of fuel cells: from conventional fuel cells to nano fuel cells, Nanotechnology in Fuel Cells. 77-21, Elsevier, 2022, https://doi.org/10.1016/B978-0-323-85727-7.00015-1
46. J.T. Gostick et al., OpenPNM: a pore network modeling package, Comput. Sci. Eng. 18 (2016) 60-74, 10.1109/MCSE.2016.49
47. M. Aghighi, J.T. Gostick, Pore network modeling of phase change in PEM fuel cell fibrous cathode, J. Appl. Electrochem. 47 (2017) 1323-1338, https://doi.org/10.1007/s10800-017-1126-6
48. J. Hack et al., X-ray micro-computed tomography of polymer electrolyte fuel cells: what is the representative elementary area?, J. Electrochem. Soc. 167 (2020) 013545, https://doi.org/10.1149/1945-7111/ab6983
49. D. Zapardiel, P.A. García-Salaberri, Modeling the interplay between water capillary transport and species diffusion in gas diffusion layers of proton exchange fuel cells using a hybrid computational fluid dynamics formulation, J. Power Sources 520 (2022) 230735, https://doi.org/10.1016/j.jpowsour.2021.230735
50. P.K. Das et al., Effective transport coefficients in PEM fuel cell catalyst and gas diffusion layers: Beyond Bruggeman approximation, Appl. Energy 87 (2020) 2785-2796, https://doi.org/10.1016/j.apenergy.2009.05.006
51. M. Ahadi et al., Thermal conductivity of catalyst layer of polymer electrolyte membrane fuel cells: Part 2–Analytical modeling, J. Power Sources 354 (2017) 215-228, https://doi.org/10.1016/j.jpowsour.2017.03.100
52. I.V. Zenyuk et al., Understanding impacts of catalyst-layer thickness on fuel-cell performance via mathematical modeling, J. Electrochem. Soc. 163 (2016) F691, https://doi.org/10.1149/2.1161607jes
53. J. Wu et al., Diagnostic tools in PEM fuel cell research: Part I Electrochemical techniques, Int. J. Hydrog. Energy 33 (2008) 1735-1746, https://doi.org/10.1016/j.ijhydene.2008.01.013
54. J. Wu et al., Diagnostic tools in PEM fuel cell research: Part II: Physical/chemical methods, Int. J. Hydrog. Energy 33 (2008) 1747-1757, https://doi.org/10.1016/j.ijhydene.2008.01.020
55. M. Schulze et al., Segmented cells as tool for development of fuel cells and error prevention/prediagnostic in fuel cell stacks, J. Power Sources 173 (2007) 19-27, https://doi.org/10.1016/j.jpowsour.2007.03.055
56. P. Boillat et al., Neutron imaging of fuel cells–Recent trends and future prospects, Curr. Opin. Electrochem. 5 (2017) 3-10, https://doi.org/10.1016/j.coelec.2017.07.012
57. I.V. Zenyuk, Bridging X-ray computed tomography and computational modeling for electrochemical energy-conversion and–storage, Curr. Opin. Electrochem. 13 (2019) 78-85, https://doi.org/10.1016/j.coelec.2018.10.016

58. A. Ozden et al., A review of gas diffusion layers for proton exchange membrane fuel cells—With a focus on characteristics, characterization techniques, materials and designs, Prog. Energy Combust. Sci. 74 (2019) 50-102, https://doi.org/10.1016/j.pecs.2019.05.002
59. N. Zamel, X. Li, Effective transport properties for polymer electrolyte membrane fuel cells–with a focus on the gas diffusion layer, Prog. Energy Combust. Sci. 39 (2013) 111-146, https://doi.org/10.1016/j.pecs.2012.07.002
60. R.R. Rashapov et al., Characterization of PEMFC gas diffusion layer porosity, J. Electrochem. Soc. 162 (2015) F603, https://doi.org/10.1149/2.0921506jes
61. S. Shukla et al., Determination of PEFC gas diffusion layer and catalyst layer porosity utilizing Archimedes principle, J. Electrochem. Soc. 166 (2019) F1142, https://doi.org/10.1149/2.0251915jes
62. J.T. Gostick et al., Capillary pressure and hydrophilic porosity in gas diffusion layers for polymer electrolyte fuel cells, J. Power Sources 156 (2006) 375-387, https://doi.org/10.1016/j.jpowsour.2005.05.086
63. T. Suzuki et al., Investigation of porous structure formation of catalyst layers for proton exchange membrane fuel cells and their effect on cell performance, Int. J. Hydrog. Energy 41 (2016) 20326-20335, https://doi.org/10.1016/j.ijhydene.2016.09.078
64. D.L. Wood et al., Surface properties of PEMFC gas diffusion layers, J. Electrochem. Soc. 157 (2009) B195, https://doi.org/10.1149/1.3261850
65. C.P. Liu et al., Measurement of Contact Angles at Carbon Fiber–Water–Air Triple-Phase Boundaries Inside Gas Diffusion Layers Using X-ray Computed Tomography, ACS Appl. Mater. Interfaces 13 (2021) 20002-20013, https://doi.org/10.1021/acsami.1c00849
66. J.J. Conde et al., Mass-transport properties of electrosprayed Pt/C catalyst layers for polymer-electrolyte fuel cells, J. Power Sources 427 (2019) 250-259, https://doi.org/10.1016/j.jpowsour.2019.04.079
67. M.M. Gomaa et al., Crosslinked PVA/SSA proton exchange membranes: correlation between physiochemical properties and free volume determined by positron annihilation spectroscopy, Phys. Chem. Chem. Phys. 20 (2018) 28287-28299, https://doi.org/10.1039/C8CP05301D
68. R.R. Rashapov, J.T. Gostick, In-plane effective diffusivity in PEMFC gas diffusion layers, Transp. Porous Media 115 (2016) 411-433, https://doi.org/10.1007/s11242-016-0648-4
69. P. Mangal et al., Experimental study of mass transport in PEMFCs: Through plane permeability and molecular diffusivity in GDLs, Electrochim. Acta 167 (2015) 160-171, https://doi.org/10.1016/j.electacta.2015.03.100
70. E. Sadeghi et al., A novel approach to determine the in-plane thermal conductivity of gas diffusion layers in proton exchange membrane fuel cells, J. Power Sources 196 (2011) 3565-3571, https://doi.org/10.1016/j.jpowsour.2010.11.151
71. A. Drobnik et al., Some aspects of the application of the laser flash method for investigations on the thermal diffusivity of porous materials, Laser Technology III 1391 (1991) 361-369, https://doi.org/10.1117/12.57190
72. X.Z. Yuan et al., Development of a 3-in-1 device to simultaneously measure properties of gas diffusion layer for the quality control of proton exchange membrane fuel cell components, J. Power Sources 477 (2020) 229009, https://doi.org/10.1016/j.jpowsour.2020.229009
73. N. Ureña et al., On the Conductivity of Proton-Exchange Membranes Based on Multiblock Copolymers of Sulfonated Polysulfone and Polyphenylsulfone: An Experimental and Modeling Study, Polymers 13 (2021) 363, https://doi.org/10.3390/polym13030363
74. J.T. Gostick et al., Direct measurement of the capillary pressure characteristics of water–air–gas diffusion layer systems for PEM fuel cells, Electrochem. Commun. 10 (2008) 1520-1523, https://doi.org/10.1016/j.elecom.2008.08.008

75. A.D. Santamaria et al., Liquid-water interactions with gas-diffusion-layer surfaces, J. Electrochem. Soc. 161 (2014) F1184, https://doi.org/10.1149/2.0321412jes
76. A. Kusoglu, A.Z. Weber, New insights into perfluorinated sulfonic-acid ionomers, Chem. Rev. 117 (2017) 987-1104, https://doi.org/10.1021/acs.chemrev.6b00159
77. J. Kleemann et al., Characterisation of mechanical behaviour and coupled electrical properties of polymer electrolyte membrane fuel cell gas diffusion layers, J. Power Sources 190 (2009) 92-102, https://doi.org/10.1016/j.jpowsour.2008.09.026
78. M.N. Silberstein, M.C. Boyce, Constitutive modeling of the rate, temperature, and hydration dependent deformation response of Nafion to monotonic and cyclic loading, J. Power Sources 195 (2010) 5692-5706, https://doi.org/10.1016/j.jpowsour.2010.03.047
79. F. Jaouen et al., Oxygen reduction activities compared in rotating-disk electrode and proton exchange membrane fuel cells for highly active FeNC catalysts, Electrochim. Acta 87 (2013) 619-628, https://doi.org/10.1016/j.electacta.2012.09.057
80. K.C. Neyerlin et al., Study of the exchange current density for the hydrogen oxidation and evolution reactions, J. Electrochem. Soc. 154 (2007) B631, https://doi.org/10.1149/1.2733987
81. K.C. Neyerlin et al., Determination of catalyst unique parameters for the oxygen reduction reaction in a PEMFC, J. Electrochem. Soc. 153 (2006) A1955, https://doi.org/10.1149/1.2266294